Acta Materialia 165 (2019) 709–721

Contents lists available at ScienceDirect

Acta Materialia

journal homepage: www.elsevier.com/locate/actamat

Full length article

Indentation of a plastically deforming metal crystal with a self-affine rigid surface: A dislocation dynamics study

S.P. Venugopalan [a, *], L. Nicola [a, b, **]

[a] Department of Material Science and Engineering, Delft University of Technology, the Netherlands
[b] Department of Industrial Engineering, University of Padova, I-35131, Padua, Italy

ARTICLE INFO

Article history:
Received 6 July 2018
Received in revised form
10 October 2018
Accepted 10 October 2018
Available online 15 October 2018

Keywords:
Contact mechanics
Self-affine surfaces
Plasticity
Dislocation dynamics

ABSTRACT

Although indentation of elastic bodies by self-affine rough indenters has been studied extensively, little attention has so far been devoted to plasticity. This is mostly because modeling plasticity as well as contact with a self-affine rough surface is computationally quite challenging. Here, we succeed in achieving this goal by using Green's function dislocation dynamics, which allows to describe the self-affine rough surface using wavelengths spanning from 5 nm to 100 μm. The aim of this work is to gain understanding in how plastic deformation affects the contact area, contact pressure and hardness, gap profile and subsurface stresses, while the roughness of the indenter is changed. Plastic deformation is found to be more pronounced for indenters with larger root-mean-square height and/or Hurst exponent, and to be size dependent. The latter means that it is not possible to scale observables, as typically done in elastic contact problems. Also, at a given indentation depth (interference) the contact area is smaller than for the corresponding elastic contact problem, but gap closure is more pronounced. Contact hardness is found to be much larger than what reported by classical plasticity studies. Primarily, this is caused by limited dislocation availability, for which the stiffness of the deforming crystal is in between that of a linear elastic and an elastic-perfectly plastic material. When calculating hardness and nominal contact pressure, including very small wavelength in the description of the surface is not necessary, because below a given wavelength the subsurface stresses become invariant to a further decrease in true contact area. This is true for both elastic and plastic materials. Considering small wavelengths is instead required to capture accurately roughening and contact stress distribution.

1. Introduction

Contact between surfaces under moderate load involves only a fraction of the surface asperities, given that most surfaces, even when visually flat, have a self-affine fractal character [1–9]. The change in contact area and local stress distribution when the surfaces are pressed into contact determines phenomena such as friction, wear, adhesion, fretting and contact fatigue. However, experimentally, it is very challenging to measure local changes in contact area, especially when the surfaces are non transparent, as in the case of metals, which is the material of interest in this study.

Recently, much effort has been devoted to the numerical modeling of rough surface contacts. In virtue of advances in numerical techniques it is now possible to model the self-affinity of surfaces incorporating a wide range of length scales. These modeling techniques include the biconjugate-gradient stabilized method [10], the boundary-element approach [11–14], the fast-Fourier-transform based boundary-value methods (FFT-BVM) [15,16] and Green's function molecular dynamics (GFMD) [17–20]. Studies using these methods have so far mostly focused on describing contact between bodies that behave elastically. However, the assumption that bodies behave elastically during contact is only valid as long as the stress in the body is mostly hydrostatic, i.e. when the bodies are nearly in full contact, or when the root-mean-square (rms) height of the rough surface or its Hurst exponent are very small. All these conditions are not met by metal surfaces, which require extremely high loads to reach full closure, have rms height ranging from 0.3 μm to 2.5 μm [8] and have Hurst exponent ranging from 0.3 to 0.9 [2,6–9], depending on the finishing. Rough metal bodies are therefore expected to deform

* Corresponding author.
** Corresponding author. Department of Material Science and Engineering, Delft University of Technology, the Netherlands.
E-mail addresses: syam.venugopal@gmail.com (S.P. Venugopalan), l.nicola@tudelft.nl (L. Nicola).

https://doi.org/10.1016/j.actamat.2018.10.020

plastically under rather moderate load. The main objective of this work is to study the plastic response of metal crystals indented by a self-affine rigid surface and investigate how their behavior differs from that of elastically deforming bodies. To this end we will use a modeling technique, Green's function dislocation dynamics, which accurately captures deformation of the rough surface, as well as dislocation plasticity in a two-dimensional framework [21].

While there is a broad literature dealing with elastic deformation of rough surfaces, much less work has been devoted to plastic deformation (see Ghaednia et al. [22] for a recent review). The first elasto-plastic contact model was proposed by Chang, Etsion and Bogy [23] and was based on the conservation of volume of the plastically deforming asperities. At a critical interference value, the material would switch from the fully elastic to the fully plastic regime. The model, although improved by Zhao et al. [24] to include an intermediate elasto-plastic regime, has the drawback that ignores interaction between asperities. The interaction is naturally captured in the work of Gao et al. [25,26], who studied elasto-plastic contact between sinusoidal surfaces and surfaces with a Weierstrass profile. These studies showed that the pressure to cause complete contact between surfaces can reach a value 5.8 times larger than the yield strength of the bulk material σ_Y, thus larger than the hardness of an isolated asperity modeled by classical plasticity (about $3\sigma_Y$). This is in consistence with the findings of Pei *et al.* [27] who modeled indentation of a flat body, deforming according to J_2 plasticity, indented by a self-affine fractal rigid surface. They argued that it is the interaction between asperities that brings the mean contact pressure p_m above the single asperity hardness. Both the work of Gao *et al.* [25] and of Pei *et al.* [27] were based on classical plasticity and therefore ignored size effects, which are found to play an important role at the micro-scale [28–33]. Due to size-dependent plasticity, metals are found to be harder to indent for decreasing size of the indenter and of the indentation depth [34–36]. One can therefore expect that size-dependent plasticity would also affect the response of rough metal surfaces upon contact, especially when interference is small. Discrete dislocation dynamics simulations can well capture size effects and will enable us in this work to assess their influence on the contact response of rough surfaces. Also, the simulations provide the subsurface stress fields, which are of great importance in determining the critical locations where dislocation-driven failure mechanisms can occur.

Discrete dislocation plasticity simulations of contact were already performed for very simple surfaces: indentation or shearing by isolated indenters in two- [37–40] and three-dimensions [41,42], periodic arrays of flat indenters [43,44] and flattening of sinusoidal surfaces [39,45–47]. These simulations confirm that for these very simple geometries the plastic response is size dependent. Dislocation dynamics simulations of contact are computationally rather expensive even in two dimensions, therefore the contact problem between self-affine surfaces, which require a fine discretization to capture a broad range of wavelength, was not attempted so far. However, Yin *et al.* [48] presented dislocation dynamics simulations for an indenter made of Hertzian asperities of different size, to simulate the effect of multiscale roughness and showed that rougher asperities induce more plasticity than smooth ones, and that subsurface stresses and dislocation densities strongly increase with interference. Recently, we presented a new version of two-dimensional discrete dislocation plasticity based on the formulation of Van der Giessen and Needleman [49] that uses Green's function molecular dynamics to compute the image fields, and by that provides a significant gain in computational speed [21]. Thanks to this method we can now model indentation with a self-affine rough indenter of a crystal deforming by dislocation plasticity to gain a better understanding of the effect of roughness parameters such as rms height, Hurst exponent, and short wavelength cut-off, by keeping track of the evolution of the contact area, of the tractions and subsurface stresses.

The remainder of the paper starts with the formulation of the problem in section 2. Then the GFDD methodology is briefly presented in 2.1, more details can be found in Ref. [21]. The way in which the surfaces are generated is given in section 2.2. The parameters chosen for the GFDD simulations are listed in section 2.3. In section 3.1, the loading rate is determined at which the GFDD simulations can be considered quasi-static. In section 3.2 the size dependence of self-affine plastic indentation is demonstrated. The effect of rms height and Hurst exponent on the contact pressure and area are presented in section 3.3. The effect of short wavelength cut-off on the contact deformation of elastic and plastic crystals is shown in section 3.4. The area–load dependency for the elasto-plastic crystal is presented in section 3.5.

2. Formulation of the problem

The schematic representation of the metal crystal indented by a rigid rough surface is shown in Fig. 1.

Indentation is performed by specifying the displacement rate of the rigid indenter $\dot{u}_z$. The top surface of the crystal is taken to be frictionless at the points of contact, $\sigma_{xz}(x_c, z_c) = 0$, and traction-free elsewhere, $\sigma_{xz}(x_{nc}, z_{nc}) = \sigma_{zz}(x_{nc}, z_{nc}) = 0$. The subscripts 'c' and 'nc' stand for 'points in contact' and 'points not in contact', respectively.

The bottom of the unit cell, $z = 0$ is fixed: $u_x(x, 0) = u_z(x, 0) = 0$.

Following [49] the crystal is initially dislocation free, and contains a given density of slip planes, dislocation sources, and obstacles. When the stress in the body is sufficiently high, dislocation dipoles are nucleated from the sources and glide on the slip planes, by that reducing the stress in the body. Each dislocation source nucleates a dipole when subjected to a resolved shear stress exceeding its critical strength, τ_{nuc}, for a given amount of time, t_{nuc}. Each dislocation source can emit multiple dipoles. The velocity with which dislocations glide is controlled by the Peach-Koehler force acting on them. Dislocations are stopped by the obstacles, but released when the resolved shear stress on them exceeds the critical strength associated to the obstacle, τ_{obs}.

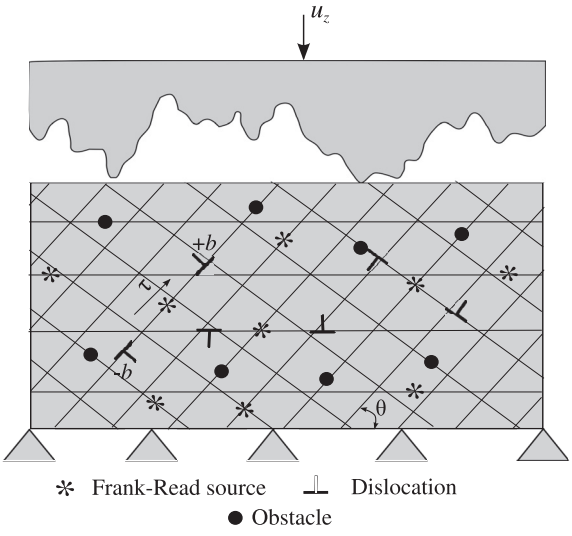

Fig. 1. Schematic representation of the metal crystal indented by a rough surface.

2.1. Solution through Green's function dislocation dynamics

The solution at each time step of the simulation is obtained by the superposition of two linear elastic solutions: The elastic analytical fields for dislocations in a homogeneous infinite solid, and the solution to the complementary elastic boundary-value problem, which corrects for the boundary conditions [49]. The latter is obtained through Green's function molecular dynamics (GFMD) [20]. The methodology is illustrated in Fig. 2 for the indentation of a single crystal by a rigid indenter with self-affine surface topography. The elastic dislocation fields are represented by the superscript (^{d}), the fields solving the complementary boundary-value problem by the superscript ($\hat{}$).

GFMD is a boundary-value method to study the elastic response of a body subjected to contact loading [20,21,50]. In GFMD, only the surface of the deformable body is modeled explicitly and discretized using nx equi-spaced grid points. The rough surface is assumed to obey the small slope approximation. The interfacial interaction adopted here is the simplest possible: in normal direction a hard-wall constraint is imposed to avoid interpenetration, and in tangential direction the contact is assumed to be frictionless. This is achieved by letting the contact points oscillate laterally to equilibrium without any constraint. It is possible to use more sophisticated interfacial interactions, for instance traction–separation laws that allow for the coupling between normal and tangential separation [51], but in this work we have chosen to focus on plasticity instead of on the interfacial behavior.

The unknown surface displacement fields $\tilde{\boldsymbol{u}}(q) = (\tilde{u}_1(q), \tilde{u}_3(q))$ for each mode with wavenumber q are calculated in Fourier space using damped dynamics. The advantage of damping the system in Fourier space is that the different modes describing the surface are uncoupled. The static solution is found using damped dynamics, while the body fields are calculated from the surface fields using closed-form analytical solutions [21].

2.2. Generation of the rough surface

The periodic self-affine surface topography for an indenter with Gaussian height distribution is generated with the power spectral density method [18]. The self-affine surfaces are constructed by generating the Fourier coefficients of the height profile as:

$$\tilde{h}(q) = h_0\, \tilde{\Delta}_G(q)\sqrt{C_h(q)} = h_0\, \frac{\tilde{\Delta}_G(q)}{q^{\left(\frac{1}{2}+H\right)}}, \tag{1}$$

where h_0 is a real-valued constant which can be adjusted to obtain the aspired rms slope of the surface, $\tilde{\Delta}_G(q)$ is a Gaussian random variable with random phase such that $\langle \tilde{\Delta}_G(q) \rangle = 0$, $C_h(q)$ is the surface height spectrum corresponding to a wave number q, and H is the Hurst exponent. The real and imaginary parts of the Gaussian random variable $\tilde{\Delta}_G(q) = \mathscr{R}\{\tilde{\Delta}_G(q)\} + i\mathscr{I}\{\tilde{\Delta}_G(q)\}$ are found from a real-valued Gaussian sequence $G[n]$ of finite length nx as:

$$\mathscr{R}\left\{\tilde{\Delta}_G(q)\right\} = \frac{1}{nx}\sum_{n=0}^{nx} G[n]\cos qn,$$

$$\mathscr{I}\left\{\tilde{\Delta}_G(q)\right\} = \frac{1}{nx}\sum_{n=0}^{nx} G[n]\sin qn. \tag{2}$$

The power-law scaling for the surface height spectrum applies between cut-offs at long and short wave numbers $q_0 < q < q_s$, where $q_0 = 2\pi/\lambda_l$ and $q_s = 2\pi/\lambda_s$ are the wavenumbers corresponding to the long and short wavelengths λ_l and λ_s (see Fig. 3). The rms height $\overline{h}$ and rms gradient $\overline{g}$ of the surface are

$$\begin{aligned} \overline{h}^2 &= \frac{1}{nx}\sum_{\mathbf{q}} |\tilde{h}(\mathbf{q})|^2 \\ \overline{g}^2 &= \frac{1}{nx}\sum_{\mathbf{q}} q^2 |\tilde{h}(\mathbf{q})|^2. \end{aligned} \tag{3}$$

For different realizations of the rough surface, all parameters, including the cut-off values, are kept fixed except the Gaussian random variable $\tilde{\Delta}_G(q)$ whose phase is randomly varied.

Before starting the simulation the surfaces so generated are shifted such that the lowest point touches the substrate at zero interfacial pressure.

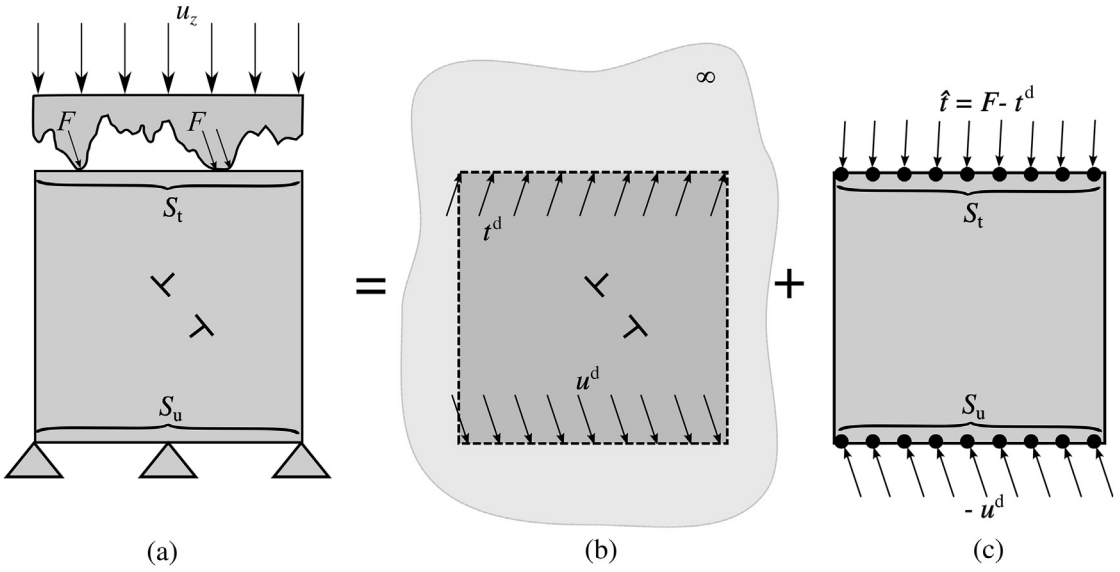

Fig. 2. (a) Schematic representation of the dislocated crystal indented by a rigid rough body. The bottom of the crystal is fixed while the indenter is pressed into contact by applying a constantly increasing displacement which gives rise to interfacial tractions, F. The solution is obtained by superposing (b) the elastic fields of the dislocations in an infinite medium and (c) the solution to the elastic boundary-value problem which corrects for the boundary conditions.

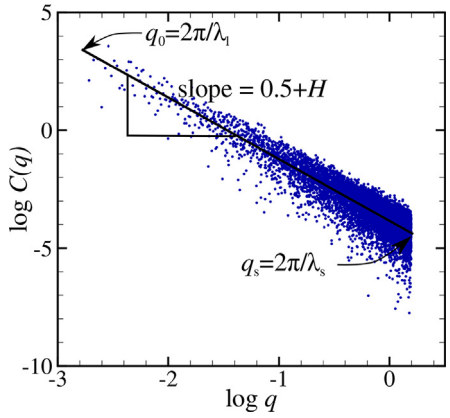

Fig. 3. Power spectral density with Gaussian distribution generated numerically for a given realization.

2.3. Choice of parameters

In this section the default parameters used in the simulations are listed.

The height of the crystal is chosen to be $z_m = 10\ \mu$m, which is sufficiently large that dislocations do not interact with the bottom of the crystal and sufficiently small to guarantee that plastic deformation occurs at small interference.

The elastic constants are taken to represent aluminum: the Young's modulus is $E = 70$ GPa and Poissons ratio $\nu = 0.33$. The dislocations can glide on three sets of parallel slip planes, orientated at: 0°, 60° and 120° with the bottom surface. The discrete slip planes are spaced at $100b$ where $b = 0.25$ nm is the length of Burger's vector. The Frank-Read sources and obstacles are randomly distributed in the crystal with a density $\rho_{nuc} = 40\ \mu m^{-2}$ and $\rho_{obs} = 40\ \mu m^{-2}$. The average source spacing $L_{ave} = \sqrt{1/\rho_{nuc}} = 158$ nm. The strength of the sources follows a Gaussian distribution with mean strength $\tau_{nuc} = 50$ MPa and standard deviation of 10 MPa. The critical time for nucleation is $t_{nuc} = 10$ ns. The strength of the obstacles is taken to be $\tau_{obs} = 150$ MPa. Dislocations of opposite sign in the same slip plane annihilate when the distance between them is below $L_{ann} = 6b$. The time step required to properly capture the dislocation interactions is found to be $\Delta t = 2.5$ ns.

In GFMD, the center-of-mass mode is critically damped or slightly under-damped for quick convergence. The damping factor is

$$\eta \propto \frac{1}{\tau}\sqrt{\left(\frac{E}{2(1+\nu)}\right)\left(\frac{L_x}{z_m\, nx}\right)}, \tag{4}$$

where $\tau = 0.25$ is the dimensionless time step used for the damped dynamics. The number of iterations to reach convergence scales as

$$n_{it} \propto \sqrt{\left(\frac{2(1+\nu)}{E}\right)\left(\frac{z_m\, nx}{L_x}\right)}. \tag{5}$$

The values for the thermodynamic, fractal and continuum (TFC) discretizations, unless otherwise stated, are $\varepsilon_t = 2^{-1}$, $\varepsilon_f = 512^{-1}$ and $\varepsilon_c = 32^{-1}$. The fractal discretization, $\varepsilon_f = \lambda_s/\lambda_l$, defines the number of wavelengths used to describe the surface. Here, the long wavelength cut-off is kept constant, i.e. $\lambda_l = 10\ \mu$m and the short wavelength cut-off varied to assess the effect of small features on the plastic response of the crystal. The thermodynamic discretization is defined as $\varepsilon_t = \lambda_l/L_x$, where L_x is the width of the periodic unit cell. In the limiting case of $\varepsilon_t \to 0$, which corresponds to the thermodynamic limit, the surface is no longer periodic since $L_x \to \infty$. Finally, the continuum discretization is defined as $\varepsilon_c = a_0/\lambda_s$ where a_0 is the spacing between the grid points that discretize the surface of the substrate. In the limiting case of $\varepsilon_c \to 0$, the grid spacing $a_0 \to 0$ and hence the surface has a continuum representation, therefore the solution must converge to the continuum mechanics solution.

3. Results and discussion

3.1. Loading rate

Firstly, we determine for which loading rate the simulations can be considered quasi-static. To this end, the crystal is indented at different loading rates to a depth of 0.01 μm. The indenter is then held at constant depth until $t = 125 \times \dot{u}_z^0/\dot{u}_z$ ns, where $\dot{u}_z^0 = 4 \times 10^5\ \mu$m/s is the reference loading rate. Fig. 4 shows the change in nominal contact pressure $p_n = F/L_x$, where F is the total contact force. It can be seen that, upon loading, the response of the substrate is stiffer for higher loading rates. This is caused by the fact that the generation of dislocations is controlled by the nucleation time t_{nuc}. If the loading is fast compared with the rate of dislocation nucleation, L_{nuc}/t_{nuc}, dislocations do not have the time to nucleate, glide, and relax the pressure as much as needed. This is why for the faster loading rate used here, $\dot{u}_z^0 = 4 \times 10^5\ \mu$m/s, the loading curve is close to the elastic limit. Only when the indenter is kept fixed at final indentation depth, the dislocations have the time to be nucleated also in the crystals that were subjected to fast loading, leading to a decrease of the contact pressure. A loading rate of $\dot{u}_z^0 = 4 \times 10^3\ \mu$m/s is chosen for all our simulations since it results in a negligible relaxation of the contact pressure at constant loading.

3.2. Size effect

To assess the occurrence of plasticity size effects in self-affine indentation we scale both the size of the crystal and the rough surface topography equally in $x-$ and $z-$ direction, while keeping the realization of the rough surface unaltered. The scaling ensures that the elastic response of all crystals is identical, such that differences in the plastic response are highlighted. The smallest crystal has width $L_x = 10\ \mu$m and height $z_m = 5\ \mu$m. It is indented by a rough surface with rms height $\bar{h} = 0.05\ \mu$m. The dimensions of the other two crystals are scaled up by two and four, so is the rms roughness height of the indenter. All crystals are indented to the same strain, $u_z/z_m = 0.002$.

As expected, the curves representing nominal contact pressure versus strain are found to be indistinguishable for all elastic crystals, as can be seen in Fig. 5a. On the contrary, a size effect is

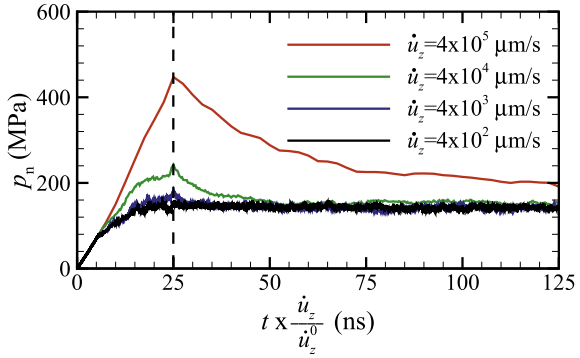

Fig. 4. Nominal contact pressure upon indentation to a depth of 0.01 μm and subsequent relaxation.

observed for the plastically deforming crystals. The thinner crystals, indented by a surface with smaller rms height, have a stiffer response upon indentation. Also, the contact area they form is larger and closer to the elastic limit (Fig. 5b). The relative contact area in Fig. 5b is defined as $a_r = A/A_0$, where A is the real contact area and A_0 is the apparent contact area. The kink in the curves Fig. 5a indicates that a new cluster of asperities has come into contact.

It is important to note here, that for a given displacement of the indenter, the contact area is smaller for plastic crystals compared to their elastic counterparts. Since the occurrence of plastic deformation reduces the interfacial force, a larger interference is required to reach the same contact area that would be reached elastically. These findings are in contradiction with the early elasto-plastic models [23,24], where contact area was expected to increase with plasticity. This is because those models are based on the incorrect assumption that the plastic contact area is given by the geometric intersection between crystal and indenter.

The normal traction t_z profiles at final strain are shown in Fig. 6. As expected, the elastic profiles overlap again, while the traction profiles become closer to the elastic solution for smaller rms height. The high peaks that characterize the profile for larger rms height are a consequence of the serrated nature of plastically deforming surfaces: the exit of dislocations leads to crystallographic steps at the surface which become more pronounced when several dislocations leave the body from the same slip plane [47]. The difference between contact pressure profiles for elastically and plastically deformed surfaces is rather pronounced: plasticity does not only lead to a smaller nominal contact pressure and true contact area, but to a very different distribution of the contact stresses. Locally the surface stresses are an order of magnitude larger than what predicted by earlier clasical plasticity study (the nucleation strength on which the tractions are magnified is of the same order as the yield strength). Consequently, also the subsurface stresses are much affected by plasticity, as shown in Fig. 7, where the stress distribution in crystals of different size are compared. Here, one can see that the size dependence is caused by dislocation source starvation in the smaller crystals: the reduced contact area is the same as in larger crystals, but the actual contact area is smaller. Therefore, the contact pressure gives rise to a smaller region affected by high stresses, where dislocations can nucleate. Because of limited source availability, the crystal with smaller dimensions exhibits less

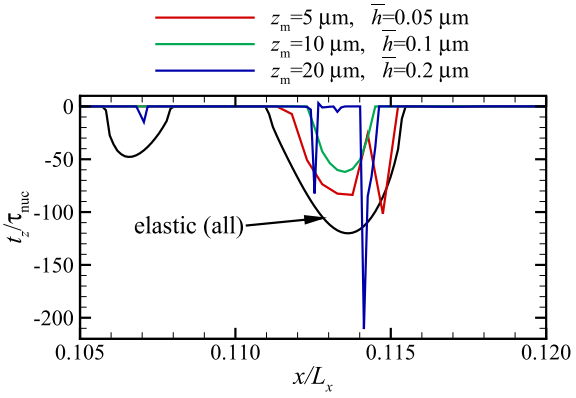

Fig. 6. Normal traction t_z profiles at strain $u_z/z_m = 0.002$ for crystals with scaled dimensions, indented by a rough surface with scaled rms height.

plasticity.

An important implication of the size-dependent response just demonstrated is that—for plastically deforming bodies—it is not possible to scale observables such as the contact pressure, the contact area, and the gap, with crystal size or rms height of the indenter, as typically done for elastic contact problems [20,52].

3.3. Effect of rms height and Hurst exponent

Here, differently from the previous section, we keep the crystal size constant and we search for the rms height that causes appreciable plasticity. At the same indentation depth a small rms height is expected to induce a more hydrostatic stress state in the subsurface, while a deviatoric stress component is needed to induce plasticity. Here, however, we focus on comparing cases that are identical from an elastic viewpoint.

Fig. 8a displays the nominal contact pressure, normalized on $\tau_{nuc}\overline{g}$, as a function of indentation depth u_z, normalized on rms height $\overline{h}$. The normalization allows for the overlapping of the elastic curves. Again, the plastic response cannot be scaled, and one can observe that the larger the rms height the larger the reduction in mean contact pressure assisted by plasticity. Although elastically at a given $u_z/\overline{h}$ the reduced pressure is the same for all cases considered, the subsurface stresses induced by different rms height differ:

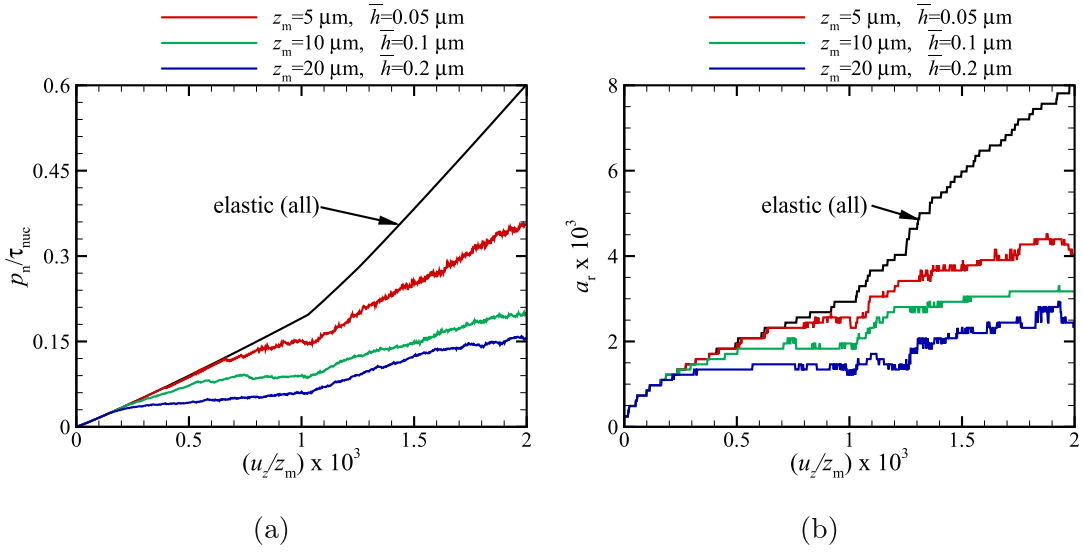

Fig. 5. (a) Nominal contact pressure and (b) relative contact area as a function of strain for crystals with scaled height indented by a rough profile with scaled rms height.

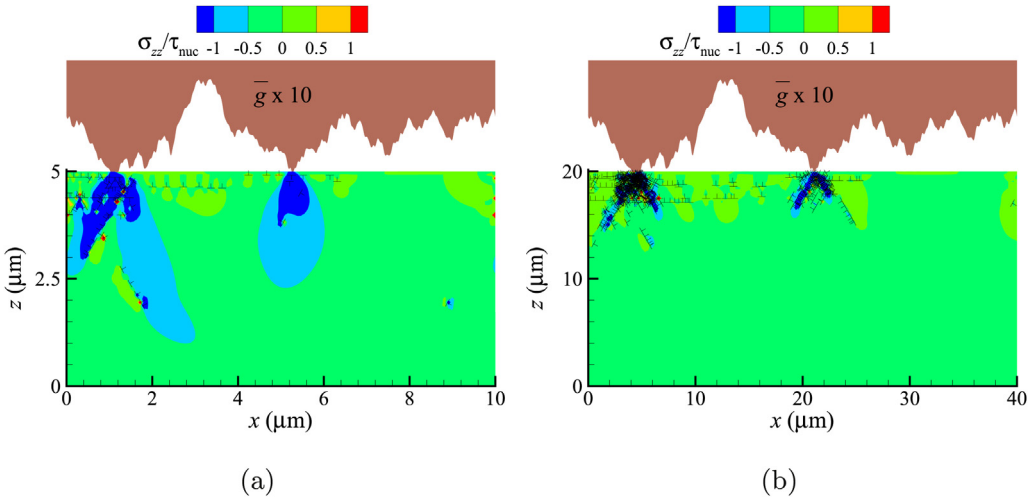

Fig. 7. Stress and dislocation distribution in two crystals with (a) $z_m = 5\ \mu m$, $\overline{h} = 0.05\ \mu m$ and (b) $z_m = 20\ \mu m$, $\overline{h} = 0.2\ \mu m$ at strain $u_z/z_m = 0.002$. The rms height of the indenter is also scaled with z_m, and magnified by a factor of 10 in $z-$ direction for better visualization.

they scale in z-direction. For a rms height of $1\ \mu m$ the plastic response is mostly pronounced because there are more dislocation sources in the deeper stressed regions, as confirmed by the dislocation density plots in Fig. 8b.

We select $\overline{h} = 0.1\ \mu m$ for all simulations in the subsequent sections, since a lower value of rms height - as generally chosen in the literature of elastic contacts [16,20,53,54]- is unrealistic for metals and induces a mostly hydrostatic stress state at rather moderate loads. A larger value of rms height violates the assumption of small-slope approximation on which the GFMD model is based, already at small indentation depth. It is however noteworthy, that metal contacts with rms height larger than what selected here are common, and they will have an even larger plastic contribution than what presented in this work.

Next, we analyze the effect of varying Hurst exponent of the indenting surface on the plastic response of the crystals, while all other surface parameters are kept constant. Experimentally measured values of the Hurst exponent for metals fall in the range of $H = 0.3$ to $H = 0.9$ depending on the material and its finishing [2,6–9].

The change in nominal contact pressure, relative contact area and dislocation density for indentation with surfaces with three different Hurst exponents $H = 0.3,\ 0.5,\ 0.8$ are presented in Fig. 9. It can be seen that for the elastic crystals, the resistance to indentation is larger for increasing values of the Hurst exponent since for a given indentation depth the smoother indenter profiles form a larger contact area with the crystal. However, for plastically deforming crystals, the contact pressure curves corresponding to different Hurst exponents tend to converge at large indentation depth such that plasticity acts as a grand equalizer, consistently to what Pei *et al.* [27] had observed. This implies that the contribution of plasticity increases with the Hurst exponent (see for confirmation Fig. 9c). This is to be expected, considering that the larger contact area induced by the indenters with larger H (see Fig. 9b) is related to a broader subsurface stressed region and therefore a greater availability of active dislocation sources.

The shear bands that form during plastic flow can be seen for $H = 0.3$ and $H = 0.8$ in Fig. 10a and b. One can see that the crystal indented by the surface with $H = 0.3$ has more, but smaller, areas of contact than the other crystal. The shear bands that form are therefore more but shorter, since they form later and they intersect, obstructing each others propagation. The crystal indented by the surface with larger Hurst exponent has a very long shear band that extends deep in the material. Notice, that these shear bands could not be captured by classical plasticity. The capability of capturing the subsurface stress distribution is very important, since it can

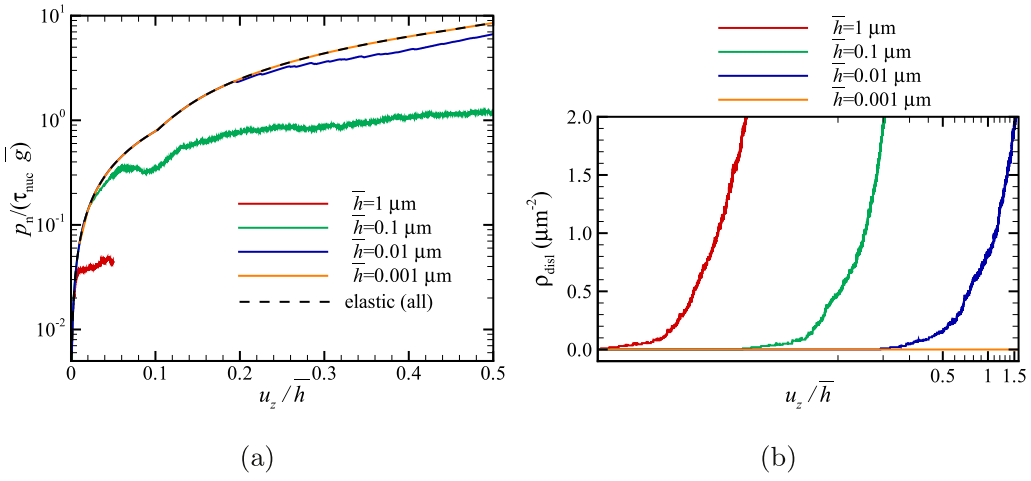

Fig. 8. (a) Normalized nominal contact pressure for different rms heights. All elastic curves overlap. Also, the curve corresponding to the plastic response of the crystal with rms height $\overline{h} = 0.001\ \mu m$ overlaps with the elastic curve, but will deviate at larger indentation depth. (b) Dislocation density ρ_{disl} in the crystal is plotted for different rms heights.

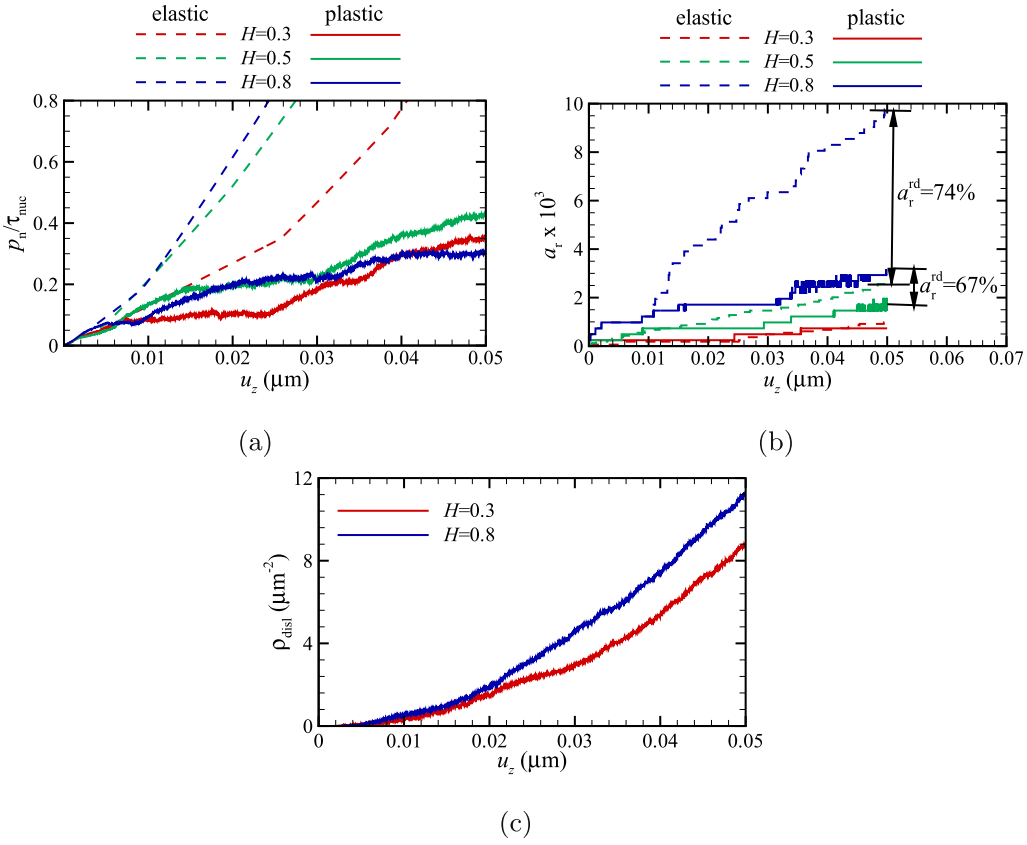

Fig. 9. (a) Nominal contact pressure (b) relative contact area, and (c) dislocation density during indentation with a rigid rough surface with various Hurst exponents.

signal initiation of failure in the material, for instance the initiation of cracks.

In all subsequent simulations, we choose a Hurst exponent $H = 0.8$ as observed on most metallic surfaces [2,6].

3.4. The short wavelength cut-off

In this section we investigate the effect of including fine roughness features on the plastic contact response, by comparing simulations in which the indenter is described using various fractal discretizations $\varepsilon_f = \lambda_s/\lambda_l$. The fractal discretization is varied by keeping the long wavelength cut-off constant and equal to 10 μm and changing the short wavelength cut-off. The largest fractal discretization $\varepsilon_f = 1$ corresponds to a sinusoidal indenter and the smallest fractal discretization $\varepsilon_f = 512^{-1}$ to wavelengths down to $\lambda_s = 19.5$ nm.

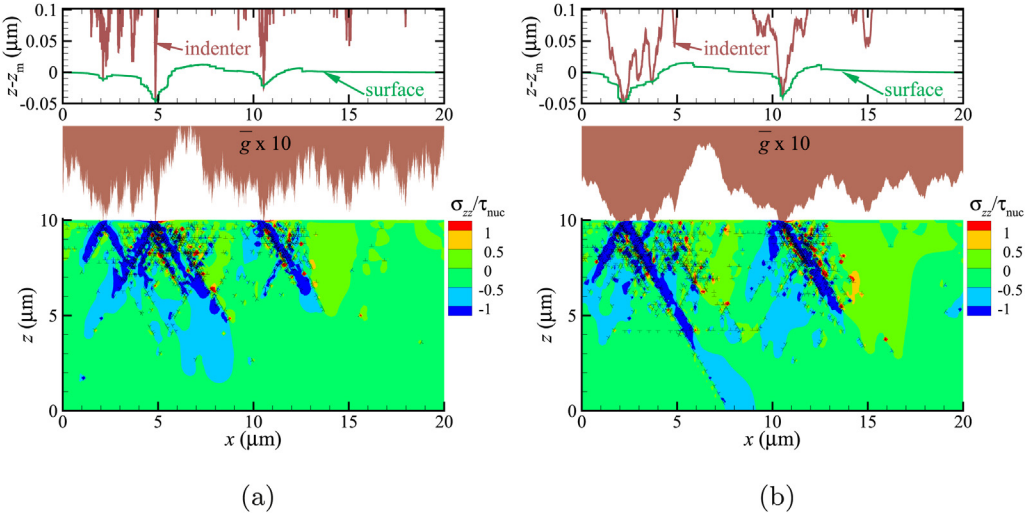

Fig. 10. Deformed surface profile (top); stress and dislocation distribution (bottom) for (a) $H = 0.3$ and (b) $H = 0.8$.

Fig. 11 shows the deformed surface after indentation to $u_z = 0.05\,\mu$m for elastic and plastic crystals. Surface profiles for $\lambda_s = 19.5$ nm and $\lambda_s = 156$ nm are compared and contrasted with those obtained by indenting with a sinusoidal surface. For the sinusoidal indentation, the contact occurs elastically over a single large patch whereas for the self-affine indenter, the contact is formed by several smaller patches. As a result, the real contact area for $\lambda_s = 156$ nm is found to be at least an order of magnitude smaller than that of sinusoidal indentation.

With plasticity, there is a pronounced material pile up in the zones surrounding the contact. This results in the surface conforming more to the indenter and hence into a significantly smaller interfacial separation. This is relevant for problems concerning the leakage of seals, where the gap between surfaces controls percolation of the fluid [55,56].

Despite interfacial separation is smaller for plasticity than for elasticity, the contact area is smaller for the plastic case, given that, at a given indentation depth, the contact pressure is reduced by plasticity. Fig. 12 shows the relative contact area at final indentation depth a_r^{fin} for different fractal discretizations. It is seen that the contact area decreases with fractal discretization for both elastic and plastic crystals with approximately the same rate. Smaller fractal discretization is characterized by asperities with smaller length scales that form contact over several smaller patches. In the case of sinusoidal indentation, the difference between elastic and plastic contact area is less. This is due to the fact that when the surface deforms plastically, dislocations exit the free surface leaving crystallographic displacement steps. This gives rise to small protrusions that make additional contact with the indenter (see Fig. 11).

The increase of contact pressure with loading is shown in Fig. 13a for various values of fractal discretization. A sudden increase in pressure is observed every time a new cluster of asperities comes into contact. For the two larger discretizations, the nominal contact pressure curves are very close, although not overlapping, neither for the elastic nor for the plastic simulations.

The results for final nominal contact pressure, normalized on source strength, are reported in Fig. 13 b for various values of the fractal discretization, i.e. various λ_s, for elastic and plastic simulations. The results lead to three main observations: (1) the data obtained with dislocation dynamics is just shifted with respect to the data obtained with elastic simulations, with plastic values being approximately 85% (for the dislocation parameters chosen in this work) smaller than the elastic values; (2) Below a threshold wavelength, $\lambda_s = 156$ nm (for the roughness parameters used in these simulations), the nominal contact pressure is unaffected by a further reduction of the short wavelength cut-off. Therefore, if one is interested in nominal contact pressure, it is not worth using a discretization smaller than this threshold value, irrespectively of whether the simulations include or not plasticity; (3) Despite true contact area always decreases with decreasing fractal discretization (see Fig. 12) nominal contact pressure does not. This means that below a given threshold for λ_s the mean contact pressure, which can be interpreted as hardness of the contact, would increase rather significantly, only because the real contact area decreases. As we will see in more detail shortly, this increase in hardness does not really reflect the physics of the problem.

Notice that we have distinguished three different domains in Fig. 13b, indicated with A, B, and C. Zone A represents the large wavelength zone, including as upper limit the sinusoidal wave. In this region the contact occurs at a single protrusion of the indenter, which becomes thinner while decreasing lambda and therefore indents the crystal meeting less resistance. There is only a continuous single contact area. In zone B, an additional decrease in wavelength is accompanied by roughening of the protruding peak which makes contact with the crystal through a couple of closely spaced contact patches, who interact elastically and effectively act as a super-contact with end-to-end distance larger than the true contact area, which always decreases with λ_s. This gives an increase in the resistance to indentation and therefore of contact pressure.

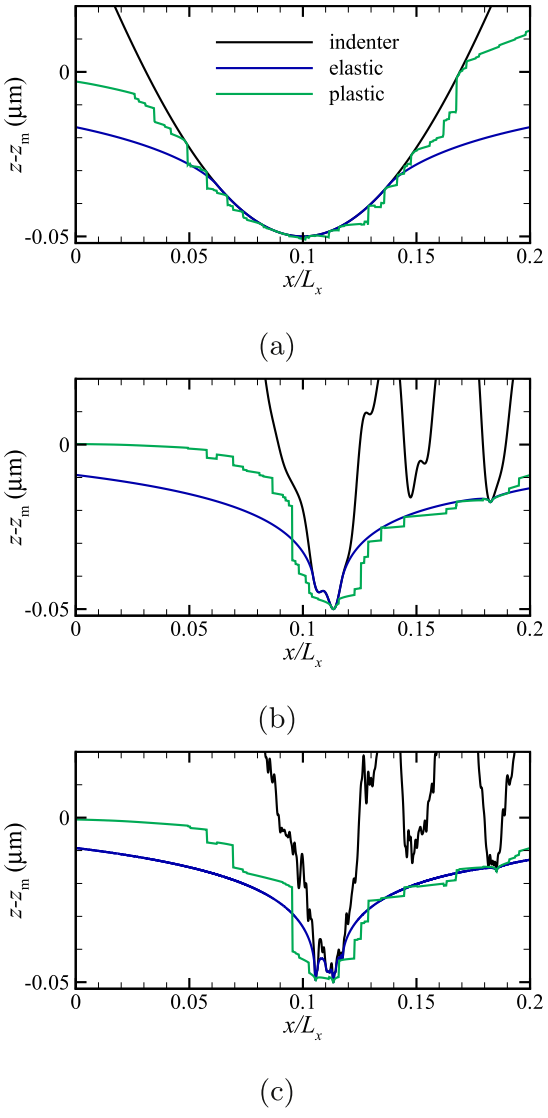

Fig. 11. Deformed surface profile at an indentation depth of 0.05 μm for (a) sinusoidal indenter and fractal indenters with (b) $\lambda_s = 156$ nm and (c) $\lambda_s = 19.5$ nm.

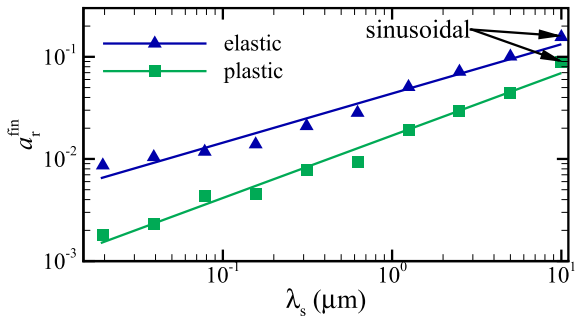

Fig. 12. Contact area at final indentation depth for different fractal discretizations.

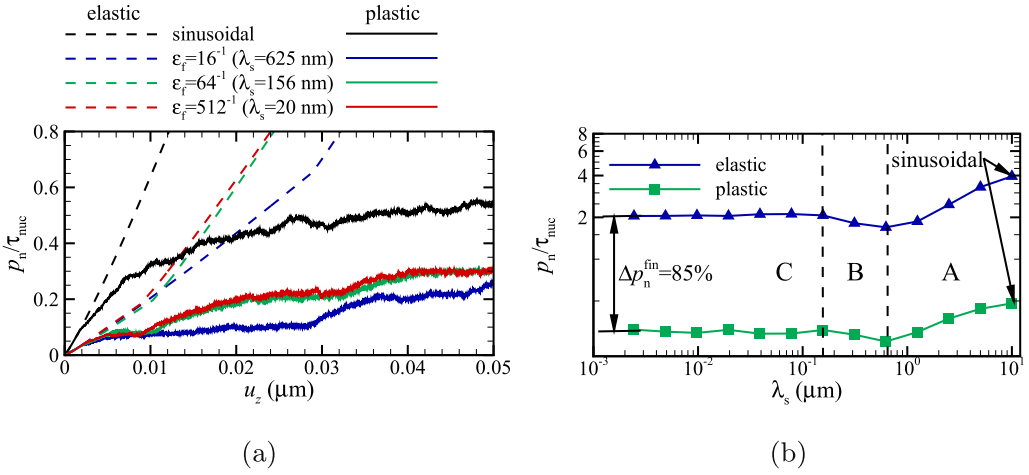

Fig. 13. (a) Evolution of contact pressure with indentation depth and (b) contact pressure at final indentation depth, for elastic and plastically deformed crystals and various values of the fractal discretization.

In zone C, decreasing wavelength further, corresponds to additional fragmentation of the already very small and closely spaced contact patches. This fragmentation decreases the true contact area further, but does not affect the stressed region in the subsurface, and does therefore not change the nominal contact pressure. This is demonstrated in Fig. 14 for $\lambda_s = 156$ nm and 19.5 nm. It can be seen that, although the true contact areas are different, in virtue of the elastic interactions, the subsurface stresses are comparable. This implies that (1) measuring or calculating true contact area below a critical threshold wavelength is not useful to determine the mechanical response (even elastic response) of the contact and (2) the quantity that is important to determine the mean contact pressure (or contact hardness) is not the true contact area, but the effective contact area, indicated in Fig. 14 as AB, which is invariant below the threshold value $\lambda_s = 156$ nm.

We choose therefore the threshold value $\lambda_s = 156$ nm to present the change of mean contact pressure $p_m = F/A$ for different source densities in Fig. 15a. Here F is the interfacial force and A is the true contact area. The mean contact pressure depends rather mildly on the range of source densities chosen, and even for the largest source density considered here it is significantly larger, 35 τ_{nuc}, than what found in simulations based on classical plasticity theory [27,57], where $p_m \approx 6\,\sigma_Y$. Here σ_Y is the yield strength on tension, which for the material parameters used in our simulations, is 60 MPa, thus of the same order as the nucleation strength, $\tau_{nuc} = 50$ MPa. The reason for the difference between the prediction in mean contact pressure of Green's function dislocation dynamics and the classical plasticity simulations [27,57] is twofold: the most important is that while in classical plasticity, plastic deformation occurs at any location where the yield strength is exceeded, in dislocation dynamics plasticity is limited by the availability of dislocation sources; also, the fractal discretization considered in this work, although cut off, is smaller than that considered in Refs. [27,57]. The hardness increases as finer roughness is added to the indenter as seen in Fig. 15b, where the mean contact pressure at $u_z = 20$ nm, which we will call hardness σ_h in the following, is presented as a function of the short wavelength cut-off for $\rho_{nuc} = 40\ /\mu m^2$. The increase in hardness is mainly due to the decrease in contact area with the decrease in λ_s (see Fig. 12). Since the decrease in true contact area below $\lambda_s \leq 156$ nm was shown to not affect the subsurface stress distribution, the contact hardness should be cut off below this threshold, and the constant value σ_h^{eff} used, as indicated in Fig. 15b.

The results of this section lead us to the following conclusions that hold for both elasticity and plasticity: If one is interested in real contact area, contact traction distribution, or gap geometry, the surface must be described with great accuracy, including the shortest wavelength observed in the self-affine surface under study. This corresponds to a fractal discretization of the surface of the order of $10^3\ /\mu m (\lambda_s \approx 10$ nm). If one is instead investigating the nominal contact pressure, mean contact pressure, or residual stress distribution inside the substrate, the fractal discretization of the surface can be an order less, i.e., $10^2/\mu m$, value at which the results converge.

3.5. Area-load dependency

A quantity that has attracted much attention in the contact mechanics community is the proportionality coefficient κ, defined as $\kappa = a_r/p^*$, where p^* is the reduced pressure expressed as $p^* = p_n/E^*\overline{g}$. So far, the study of κ has been mostly limited to self-affine indentation of elastic bodies. It was shown that κ in elastic bodies follows a power law with respect to fractal discretization, i.e., $\kappa \propto \varepsilon_f^{0.67}$ [20]. Pei *et. al.* [27] performed simulations of rough surface contact using J_2 plasticity with isotropic hardening and found a larger value for κ for plasticity than for elasticity. Here we are interested to see how κ found for elastic simulations compares to that found by our dislocation dynamics simulations for various values of the fractal discretization, namely $2048^{-1} < \varepsilon_f < 1$, and whether our findings are in line with those of Pei *et. al.* [27]. Notice that the simulations in this work are two-dimensional, but it was shown that the difference in κ between 2D and 3D simulations is only about 10% [58]. Here we can unfortunately not compare directly our κ with that of Pei *et. al.* [27], because κ depends on various factors that are different in our simulations: Pei *et al.* [27] consider a softer material, a larger rms roughness, a significantly larger indentation depth, and they do not report the value of fractal discretization.

We present the evolution of relative contact area a_r with respect to the reduced pressure p^* in Fig. 16. The results are separated in two figures, one which includes the initial non-linear response and the other for the linear response at larger load. In Fig. 16b the curves for the plastically deforming crystals stop when the load reaches its maximum value, i.e. an additional increase in displacement will not lead to an increase in nominal contact pressure. Notice that, in accordance with the findings of Pei *et. al.* [27], the values of the

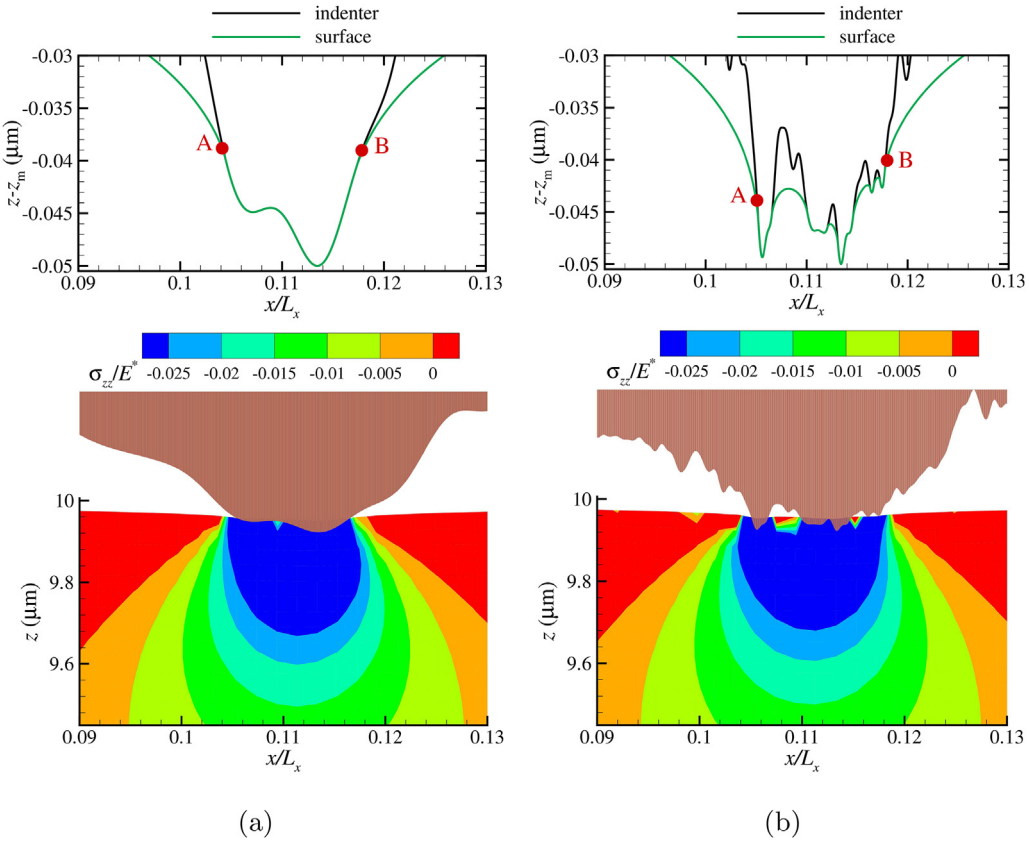

Fig. 14. Indenters and surface profiles (top) and stress distribution (bottom) for indentation using (a) $\lambda_s = 156$ nm and (b) $\lambda_s = 19.5$ nm.

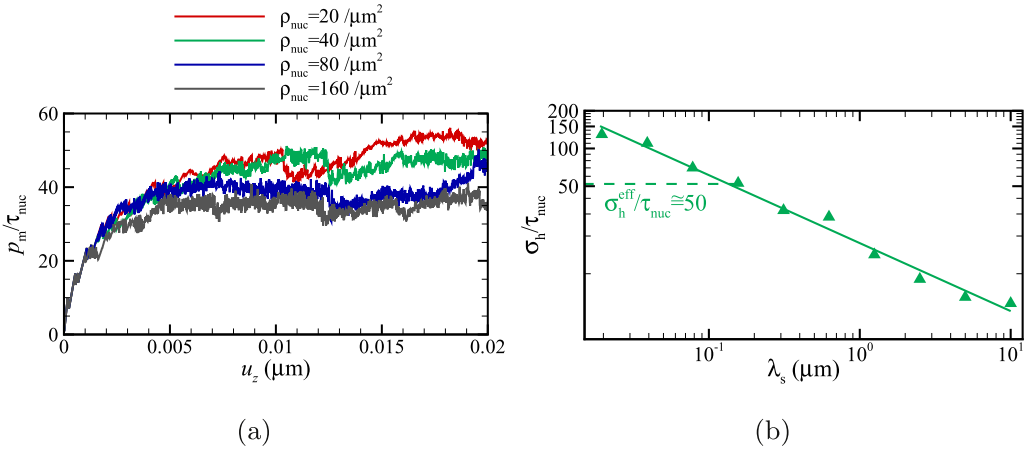

Fig. 15. (a) Mean contact pressure as a function of strain u_z/z_m for different values of source densities ρ_{nuc}. (b) Asperity hardness σ_h calculated at 0.2 % strain is plotted as a function of λ_s.

slope κ are found to be larger for plastic than elastic crystals. Thus, for a given pressure, the contact area is larger if the crystal deforms plastically. Be reminded that for a given indentation depth, the opposite holds true: the contact area is larger if the bodies deform elastically (see Fig. 12).

The dependency of the contact area fraction to the reduced pressure is found to be non-linear at the beginning of indentation ($p^* < 0.0002$) because the reduced pressure $p^* = \frac{p_n}{E^* \bar{g}}$ is here normalized, as usual, by the gradient of the indenter $\bar{g}$ whereas it is the gradient of the deformed surface $\bar{g}_c$ during indentation the quantity that determines the change of contact area with load. Therefore in the following we will use the actual gradient of the surface $\bar{g}_c$ calculated as:

$$\bar{g}_c^2 = \frac{1}{n_c}\left(\sum_{i=1}^{nx}\left(\frac{z_s^{i+1} - z_s^i}{a_0}\right)^2 \cdot \left(1 - \delta_{0,t_z^i}\right)\right), \tag{6}$$

where z_s^i is the location of the i^{th} grid point and the number of contacting points is calculated as $n_c = \sum_{i=1}^{nx}(1 - \delta_{0,t_z^i})$, where $\delta_{\alpha\beta}$ is

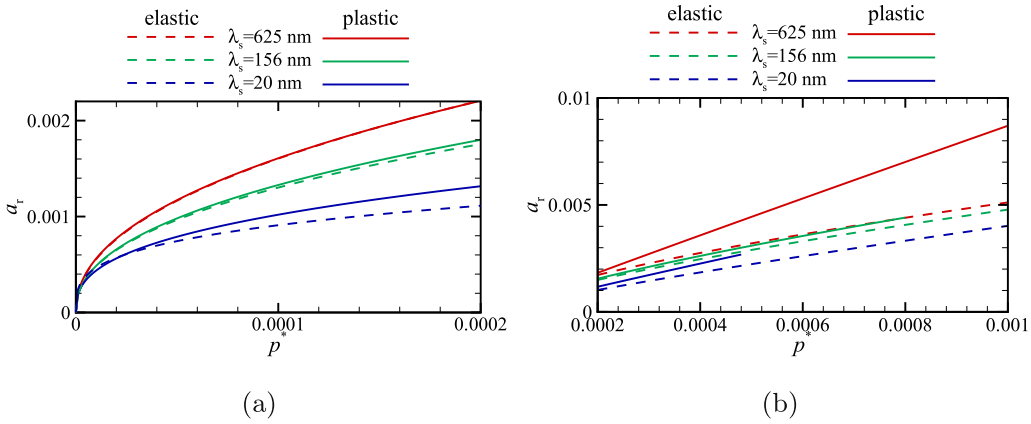

Fig. 16. Contact area vs. reduced pressure for (a) $p^* < 0.0002$ and (b) $p^* > 0.0002$.

the Kronecker delta and t_z^i is the normal traction at the i^{th} grid point. It can be seen from Fig. 17a that $\overline{g}/\overline{g}_c$ is large at small loading, causing the initial non-linear dependency. Also, the difference between $\overline{g}$ and $\overline{g}_c$ is larger for plastically deforming surfaces.[1]

In Fig. 17b one can see that using $\overline{g}_c$ instead of $\overline{g}$ results in a linear dependency of contact area on reduced pressure and all curves almost overlap leading to a universal value of $\kappa_c = 1.67 \pm 10\%$. It is noteworthy that this overlap does not indicate that there is no difference between elasticity and plasticity in terms of load-area dependency, just that this difference is now reflected in the actual gradient of the contact (see Fig. 17a).

In Fig. 18 the results for κ and κ_c are compiled for one of the realizations (a given set of sources and obstacle distribution). It can be seen that the difference in κ for the plastic and elastic crystals is lower with smaller fractal discretization. This is because the smaller the contact area the more plasticity is source limited. Here, we have also indicated a curve for κ_{eff}, which differs from κ only below the threshold $\varepsilon_f = 64^{-1}$, since, as previously demonstrated, the effective contact area which determines the stress state in the body does not change below the threshold. It is seen that $\kappa^{\text{eff}}_{\text{plas}}/\kappa^{\text{eff}}_{\text{elas}} \to 2.4$.

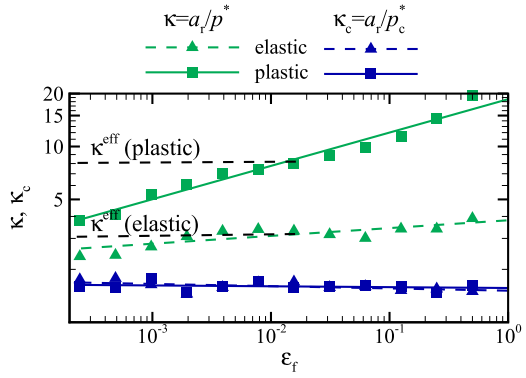

Fig. 18. κ and κ_c are plotted for different fractal discretization.

4. Concluding remarks

We modeled indentation of a metal single crystal by means of a self-affine rigid surface using Green's function dislocation dynamics (GFDD). The method provides an accurate description of

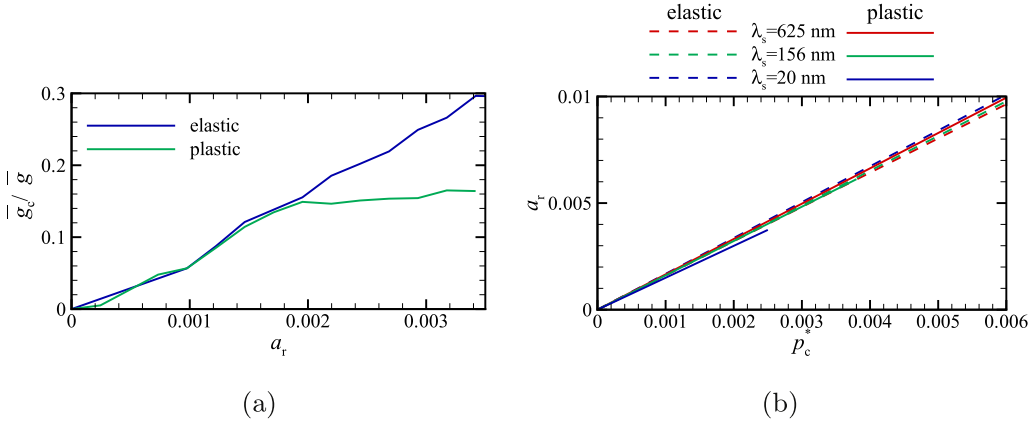

Fig. 17. (a) Evolution of local gradient with respect to contact area for indentation of an elastic and plastic crystal using an indenter with $\lambda_s = 156$ nm. (b) Contact area vs. reduced pressure p_c^* for different values of λ_s.

[1] The difference in local and overall gradient for elastic contacts is significant only for linear contacts, while for surface contacts it is negligible [58,59].

plasticity by accounting for the collective glide of discrete dislocations as well as a detailed description of the self-affine roughness. Indentation is performed with a loading rate of $\dot{u}_z = 4 \times 10^3$ μm/s, which is found to be slow enough to ensure that the simulations are quasi-static. The simulations keep track of the changing contact area, the roughening of the metal surface, the pressure distribution, and of sub-surface plastic deformation. The results of the simulations lead us to the following observations and conclusions:

- By comparing the contact response of crystals with scaled dimensions indented by self-affine rough surfaces with similarly scaled topography, it is found that, although the elastic behavior is identical, the plastic response is not. Plasticity brings in a size effect, for which larger systems (thicker crystals indented deeper by surfaces with larger dimensions) deform plastically more than smaller systems, for which dislocation nucleation is source limited. This entails that the scaling of observables typically performed for elastic contact problems is not appropriate for plastically deforming crystals.
- At a given indentation depth a body that deforms plastically forms a smaller contact area with the indenter than one that deforms elastically. However, if the comparison is made at the same nominal contact pressure, the opposite holds true.
- Plastic deformation induces material pile-up. As a consequence, although at a given interference the contact area is smaller than that of a corresponding elastic crystal, the surface is more conforming to the indenter, for which the gap closure is larger. This is of relevance in problems related to leakage.
- The rms height is an important length in contact problems involving plasticity: the larger it is, the stronger the effect of plasticity. This is not only true at constant indentation depth, because a larger rms height induces a larger deviatoric stress component in the subsurface, and therefore earlier plasticity, but also at constant u/rms-height although the elastic reduced contact pressure is the same.
- Although for elastic crystals the resistance to indentation increases with Hurst exponent, plasticity is marginally affected by *H*. At rather small interference the pressure–displacement curves for various *H* become indistinguishable. This entails that plasticity is more effective when the Hurst exponent is large.
- Indentation to an interference of 50 nm for various values of the fractal discretization has indicated that, although the actual contact area decreases with decreasing fractal discretization, the nominal contact pressure is constant below a threshold value for λ_s. We have shown that below that value, due to elastic interaction, the fragmented contact area acts as a continuous effective contact, whose length does not change with further decreasing true contact area and which causes a constant subsurface stress distribution. We conclude that if one is interested in either nominal or mean contact pressure at a given indentation, for either elastic or plastic contacts, it is not worthwhile to describe the surface with wavelengths below the threshold. In fact considering λ_s below the threshold is not only useless but deleterious: since true contact area decreases the hardness blows up, despite the subsurface stresses are invariant. On the contrary, when one is interested in real contact area, contact traction distribution, or gap geometry, the surface must be described with great accuracy, including the shortest wavelength present in the self-affine surface under study.
- The mean contact pressure (or contact hardness) at 20 nm is found to be significantly larger than in previous plasticity studies, up to 40 σ_Y, for the threshold value $\lambda_s = 156$ nm. The contact stiffness found with dislocation dynamics simulations is in between the elastic stiffness and the stiffness found by classical plasticity.
- The proportionality coefficient $\kappa = a_r/p^*$ strongly depends on fractal discretization. However, we find that $\kappa^{\text{eff}}_{\text{plas}}/\kappa^{\text{eff}}_{\text{elas}} \to 2.4$ for our choice of continuum and thermodynamic discretizations $\varepsilon_c = 32^{-1}$ and $\varepsilon_t = 2^{-1}$.

It is finally to be noted that the results presented in this work are based on a two-dimensional representation of the contact problem and cannot capture the dislocation structures that could form in three-dimensions. It is therefore not possible to estimate the effect of dislocation double cross-slip, which might be promoted by the large stresses acting in the contact regions and is observed in simulations of indentation modeled by three-dimensional dislocation dynamics [60]. Other limitations are that the model only considers small deformations and studies the behavior of a pure single crystal.

Acknowledgement

This project has received funding from the European Research Council (ERC) under the European Union's Horizon 2020 research and innovation programme (grant agreement no. 681813).

Appendix A. Supplementary data

Supplementary data related to this article can be found at https://doi.org/10.1016/j.actamat.2018.10.020.

References

[1] B.B. Mandelbrot, D.E. Passoja, A.J. Paullay, Fractal Character of Fracture Surfaces of Metals, Nature Publishing Group, 1984.
[2] E. Bouchaud, G. Lapasset, J. Planes, Fractal dimension of fractured surfaces: a universal value? EPL (Europhysics Letters) 13 (1) (1990) 73.
[3] A. Majumdar, C. Tien, Fractal characterization and simulation of rough surfaces, Wear 136 (2) (1990) 313–327.
[4] J. Krim, G. Palasantaz, Experimental observations of self-affine scaling and kinetic roughening at sub-micron lengthscales, Int. J. Mod. Phys. B 09 (06) (1995) 599–632.
[5] E. Bouchaud, Scaling properties of cracks, J. Phys. Condens. Matter 9 (21) (1997) 4319.
[6] R. Dauskardt, F. Haubensak, R. Ritchie, On the interpretation of the fractal character of fracture surfaces, Acta Metall. Mater. 38 (2) (1990) 143–159.
[7] A. Imre, T. Pajkossy, L. Nyikos, Electrochemical determination of the fractal dimension of fractured surfaces, Acta Metall. Mater. 40 (8) (1992) 1819–1826.
[8] F. Plouraboué, M. Boehm, Multi-scale roughness transfer in cold metal rolling, Tribol. Int. 32 (1) (1999) 45–57. https://doi.org/10.1016/S0301-679X(99)00013-4.
[9] F. Lechenault, G. Pallares, M. George, C. Rountree, E. Bouchaud, M. Ciccotti, Effects of finite probe size on self-affine roughness measurements, Phys. Rev. Lett. 104 (2) (2010), 025502.
[10] J.-J. Wu, Numerical analyses on elliptical adhesive contact, J. Phys. Appl. Phys. 39 (9) (2006) 1899–1907, https://doi.org/10.1088/0022-3727/39/9/027.
[11] S. Ilincic, G. Vorlaufer, P. Fotiu, A. Vernes, F. Franek, Combined finite element-boundary element method modelling of elastic multi-asperity contacts, Proc. IME J. J. Eng. Tribol. 223 (5) (2009) 767–776, https://doi.org/10.1243/13506501JET542.
[12] S. Ilincic, N. Tungkunagorn, A. Vernes, G. Vorlaufer, P. Fotiu, F. Franek, Finite and boundary element method contact mechanics on rough, artificial hip joints, Proc. IME J. J. Eng. Tribol. 225 (11) (2011) 1081–1091, https://doi.org/10.1177/1350650111406776.
[13] C. Putignano, L. Afferrante, G. Carbone, G. Demelio, A new efficient numerical method for contact mechanics of rough surfaces, Int. J. Solid Struct. 49 (2) (2012) 338–343. https://doi.org/10.1016/j.ijsolstr.2011.10.009.
[14] C. Putignano, L. Afferrante, G. Carbone, G. Demelio, The influence of the statistical properties of self-affine surfaces in elastic contacts: a numerical investigation, J. Mech. Phys. Solid. 60 (5) (2012) 973–982. https://doi.org/10.1016/j.jmps.2012.01.006.
[15] H. Stanley, T. Kato, An FFT-based method for rough surface contact, J. Tribol. 119 (3) (1997) 481–485.
[16] I. Polonsky, L. Keer, Fast methods for solving rough contact problems: a comparative study, J. Tribol. 122 (1) (2000) 36–41, https://doi.org/10.1115/1.555326.
[17] C. Campañá, M.H. Müser, Contact mechanics of real vs. randomly rough

surfaces: a Green's function molecular dynamics study, EPL (Europhysics Letters) 77 (3) (2007) 38005.
[18] C. Campañá, M.H. Müser, M.O. Robbins, Elastic contact between self-affine surfaces: comparison of numerical stress and contact correlation functions with analytic predictions, J. Phys. Condens. Matter 20 (35) (2008) 354013.
[19] W. Dapp, N. Prodanov, M. Müser, Systematic analysis of Persson's contact mechanics theory of randomly rough elastic surfaces, J. Phys. Condens. Matter 26 (35). https://doi.org/10.1088/0953-8984/26/35/355002
[20] N. Prodanov, W.B. Dapp, M.H. Müser, On the contact area and mean gap of rough, elastic contacts: dimensional analysis, numerical corrections, and reference data, Tribol. Lett. 53 (2) (2014) 433–448, https://doi.org/10.1007/s11249-013-0282-z.
[21] S.P. Venugopalan, M.H. Müser, L. Nicola, Greens function molecular dynamics meets discrete dislocation plasticity, Model. Simulat. Mater. Sci. Eng. 25 (6) (2017), 065018.
[22] H. Ghaednia, X. Wang, S. Saha, Y. Xu, A. Sharma, R.L. Jackson, A review of elastic–plastic contact mechanics, Appl. Mech. Rev. 69 (6) (2017), 060804.
[23] W. Chang, I. Etsion, D.B. Bogy, An elastic-plastic model for the contact of rough surfaces, J. Tribol. 109 (2) (1987) 257–263.
[24] Y. Zhao, D.M. Maietta, L. Chang, An asperity microcontact model incorporating the transition from elastic deformation to fully plastic flow, J. Tribol. 122 (1) (2000) 86–93.
[25] Y. Gao, A. Bower, K.-S. Kim, L. Lev, Y. Cheng, The behavior of an elastic–perfectly plastic sinusoidal surface under contact loading, Wear 261 (2) (2006) 145–154.
[26] Y.-F. Gao, A. Bower, Elastic–plastic contact of a rough surface with Weierstrass profile, Proc. Roy. Soc. Lond.: Math. Phys. Eng. Sci. 462 (2065) (2006) 319–348, https://doi.org/10.1098/rspa.2005.1563.
[27] L. Pei, S. Hyun, J. Molinari, M.O. Robbins, Finite element modeling of elasto-plastic contact between rough surfaces, J. Mech. Phys. Solid. 53 (11) (2005) 2385–2409. https://doi.org/10.1016/j.jmps.2005.06.008.
[28] N. Fleck, G. Muller, M. Ashby, J. Hutchinson, Strain gradient plasticity: theory and experiment, Acta Metall. Mater. 42 (2) (1994) 475–487. https://doi.org/10.1016/0956-7151(94)90502-9.
[29] Q. Ma, D.R. Clarke, Size dependent hardness of silver single crystals, J. Mater. Res. 10 (1995) 853–863, https://doi.org/10.1557/JMR.1995.0853.
[30] L. Nicola, E.V. der Giessen, A. Needleman, Discrete dislocation analysis of size effects in thin films, J. Appl. Phys. 93 (10) (2003) 5920–5928.
[31] J.R. Greer, W.C. Oliver, W.D. Nix, Size dependence of mechanical properties of gold at the micron scale in the absence of strain gradients, Acta Mater. 53 (6) (2005) 1821–1830.
[32] L. Nicola, Y. Xiang, J. Vlassak, E.V. der Giessen, A. Needleman, Plastic deformation of freestanding thin films: experiments and modeling, J. Mech. Phys. Solid. 54 (10) (2006) 2089–2110.
[33] C.A. Volkert, E.T. Lilleodden, Size effects in the deformation of sub-micron Au columns, Phil. Mag. 86 (33–35) (2006) 5567–5579.
[34] W. Nix, H. Gao, Indentation size effects in crystalline materials: a law for strain gradient plasticity, J. Mech. Phys. Solid. 46 (3) (1998) 411–425, https://doi.org/10.1016/S0022-5096(97)00086-0.
[35] J. Swadener, E. George, G. Pharr, The correlation of the indentation size effect measured with indenters of various shapes, J. Mech. Phys. Solid. 50 (4) (2002) 681–694.
[36] Z. Zong, W. Soboyejo, Indentation size effects in face centered cubic single crystal thin films, Mater. Sci. Eng., A 404 (1–2) (2005) 281–290.
[37] D. Balint, V. Deshpande, A. Needleman, E.V. der Giessen, Discrete dislocation plasticity analysis of the wedge indentation of films, J. Mech. Phys. Solid. 54 (11) (2006) 2281–2303.
[38] A. Widjaja, E. Van der Giessen, V. Deshpande, A. Needleman, Contact area and size effects in discrete dislocation modeling of wedge indentation, J. Mater. Res. 22 (3) (2007) 655–663, https://doi.org/10.1557/jmr.2007.0090.
[39] V. Deshpande, D. Balint, A. Needleman, E. Van der Giessen, Size effects in single asperity frictional contacts, Model. Simulat. Mater. Sci. Eng. 15 (1) (2007) 97–108, https://doi.org/10.1088/0965-0393/15/1/S09.
[40] F. Sun, E. Van der Giessen, L. Nicola, Dry frictional contact of metal asperities: a dislocation dynamics analysis, Acta Mater. 109 (2016) 162–169, https://doi.org/10.1016/j.actamat.2016.02.033.
[41] W.A. Curtin, R.E. Miller, Atomistic/continuum coupling in computational materials science, Model. Simulat. Mater. Sci. Eng. 11 (3) (2003) R33.
[42] M.C. Fivel, Discrete dislocation dynamics: an important recent break-through in the modelling of dislocation collective behaviour, Compt. Rendus Phys. 9 (3–4) (2008) 427–436.
[43] L. Nicola, A. Bower, K.-S. Kim, A. Needleman, E. Van der Giessen, Surface versus bulk nucleation of dislocations during contact, J. Mech. Phys. Solid. 55 (6) (2007) 1120–1144, https://doi.org/10.1016/j.jmps.2006.12.005.
[44] L. Nicola, A. Bower, K.-S. Kim, A. Needleman, E. Van der Giessen, Multi-asperity contact: a comparison between discrete dislocation and crystal plasticity predictions, Phil. Mag. 88 (30–32) (2008) 3713–3729, https://doi.org/10.1080/14786430802566372.
[45] F. Sun, E. Van der Giessen, L. Nicola, Plastic flattening of a sinusoidal metal surface: a discrete dislocation plasticity study, Wear 296 (2012) 672–680, https://doi.org/10.1016/j.wear.2012.08.007.
[46] F. Sun, E.V. der Giessen, L. Nicola, Interaction between neighboring asperities during flattening: a discrete dislocation plasticity analysis, Mech. Mater. 90 (Supplement C) (2015) 157–165.
[47] K. Ng Wei Siang, L. Nicola, Static friction of sinusoidal surfaces: a discrete dislocation plasticity analysis, Phil. Mag. 97 (29) (2017) 2597–2614, https://doi.org/10.1080/14786435.2017.1344785.
[48] X. Yin, K. Komvopoulos, A discrete dislocation plasticity analysis of a single-crystal semi-infinite medium indented by a rigid surface exhibiting multi-scale roughness, Phil. Mag. 92 (24) (2012) 2984–3005, https://doi.org/10.1080/14786435.2012.682178.
[49] E. Van der Giessen, A. Needleman, Discrete dislocation plasticity: a simple planar model, Model. Simulat. Mater. Sci. Eng. 3 (5) (1995) 689.
[50] S.P. Venugopalan, L. Nicola, M.H. Müser, Green's function molecular dynamics: including finite heights, shear, and body fields, Model. Simulat. Mater. Sci. Eng. 25 (3) (2017), 034001.
[51] M. Khajeh Salehani, N. Irani, M. Müser, L. Nicola, Modelling coupled normal and tangential tractions in adhesive contacts, Tribol. Int. 124 (2018) 93–101, https://doi.org/10.1016/j.triboint.2018.03.022.
[52] M.H. Müser, W.B. Dapp, R. Bugnicourt, P. Sainsot, N. Lesaffre, T.A. Lubrecht, B.N.J. Persson, K. Harris, A. Bennett, K. Schulze, S. Rohde, P. Ifju, W.G. Sawyer, T. Angelini, H. Ashtari Esfahani, M. Kadkhodaei, S. Akbarzadeh, J.-J. Wu, G. Vorlaufer, A. Vernes, S. Solhjoo, A.I. Vakis, R.L. Jackson, Y. Xu, J. Streator, A. Rostami, D. Dini, S. Medina, G. Carbone, F. Bottiglione, L. Afferrante, J. Monti, L. Pastewka, M.O. Robbins, J.A. Greenwood, Meeting the contact-mechanics challenge, Tribol. Lett. 65 (4) (2017) 118, https://doi.org/10.1007/s11249-017-0900-2. https://doi.org/10.1007/s11249-017-0900-2.
[53] B.N.J. Persson, Elastoplastic contact between randomly rough surfaces, Phys. Rev. Lett. 87 (2001) 116101, https://doi.org/10.1103/PhysRevLett.87.116101.
[54] S. Hyun, L. Pel, J. Molinari, M. Robbins, Finite-element analysis of contact between elastic self-affine surfaces, Phys. Rev. E - Stat. Nonlinear Soft Matter Phys. 70 (2 2) (2004), 026117–1–026117–12.
[55] W.B. Dapp, A. Lücke, B.N. Persson, M.H. Müser, Self-affine elastic contacts: percolation and leakage, Phys. Rev. Lett. 108 (24) (2012) 244301.
[56] F. Pérez-Ràfols, R. Larsson, A. Almqvist, Modelling of leakage on metal-to-metal seals, Tribol. Int. 94 (2016) 421–427.
[57] Y. Gao, A. Bower, K.-S. Kim, Some issues of rough surface contact plasticity at micro-and nano-scales, MRS Online Proc. Library Archive 841.
[58] J.S. van Dokkum, M. Khajeh Salehani, N. Irani, L. Nicola, On the proportionality between area and load in line contacts, Tribol. Lett. 66 (3) (2018) 115, https://doi.org/10.1007/s11249-018-1061-7. https://doi.org/10.1007/s11249-018-1061-7.
[59] M.H. Müser, On the linearity of contact area and reduced pressure, Tribol. Lett. 65 (4) (2017) 129.
[60] J. Gagel, D. Weygand, P. Gumbsch, Formation of extended prismatic dislocation structures under indentation, Acta Mater. 111 (2016) 399–406. https://doi.org/10.1016/j.actamat.2016.04.002. http://www.sciencedirect.com/science/article/pii/S1359645416302580.